Physics of the Earth and Planetary Interiors 170 (2008) 156–169

Contents lists available at ScienceDirect

Physics of the Earth and Planetary Interiors

journal homepage: www.elsevier.com/locate/pepi

Plastic deformation of wadsleyite and olivine at high-pressure and high-temperature using a rotational Drickamer apparatus (RDA)

Yu Nishihara[a,b,c,*], David Tinker[a], Takaaki Kawazoe[a], Yousheng Xu[a], Zhicheng Jing[a], Kyoko N. Matsukage[a,d], Shun-ichiro Karato[a]

[a] Department of Geology and Geophysics, Yale University, New Haven, CT 06520, USA
[b] Institute for Solid State Physics, University of Tokyo, Kashiwa, Chiba 277-8581, Japan
[c] Department of Earth and Planetary Sciences, Tokyo Institute of Technology, Meguro-ku, Tokyo 152-8551, Japan
[d] Department of Earth Sciences, Faculty of Sciences, Ibaraki University, Mito, Ibaraki 310-0056, Japan

ARTICLE INFO

Article history:
Received 30 June 2007
Received in revised form 20 February 2008
Accepted 7 March 2008

Keywords:
Wadsleyite
Olivine
rheology
Mantle transition zone
410-km discontinuity
High-pressure and high-temperature deformation experiments

ABSTRACT

Large-strain plastic deformation experiments of wadsleyite and olivine were conducted using a rotational Drickamer apparatus (RDA) up to pressure and temperature conditions corresponding to the Earth's mantle transition zone. Sintered ring-shaped $(Mg,Fe)_2SiO_4$ wadsleyite and olivine samples were deformed at $P \sim 16$ GPa and $T = 1600$ and 1800 K, and $P \sim 11$ GPa and $T = 1800$ K, respectively, with equivalent strain rate of $\dot{\varepsilon}_E \sim 6 \times 10^{-5}$ s^{-1}. In situ observations of deforming samples were carried out using the synchrotron radiation facility at Brookhaven National Laboratory, NSLS, X17B2. Stress was measured by X-ray diffraction at six different angles with respect to the compression axis. The stress estimated by X-ray diffraction was in good agreement with the stress estimated from dislocation density (for olivine). Strain was determined using X-ray radiographs of a strain marker (Re or Mo foil). Deformation of samples with a RDA involves both uniaxial compression and simple shear. A new formulation is developed to analyze both components to determine the rheological properties of a sample. Stress–strain curves show strain-hardening up to the equivalent strain of $\varepsilon_E \sim 0.2$ followed by the quasi-steady state deformation. Wadsleyite is found to be stronger than olivine compared at similar conditions and the creep strength of olivine at $P \sim 11$ GPa is much higher than those at lower pressures.

1. Introduction

The 410-km discontinuity of Earth's mantle may play a critical role in the material circulation in Earth. The olivine–wadsleyite phase transition is believed to be responsible for the discontinuity, and the changes in density and viscosity caused by the phase transformation likely have an important influence on mantle convection. The nature of density changes across 410-km discontinuity has been studied (e.g. Irifune and Ringwood, 1987) and its influence on mantle convection has been investigated (e.g. Christensen and Yuen, 1984), but another important material property, viscosity, has been largely unconstrained.

Sharp et al. (1994) reported the first results of stress relaxation tests on wadsleyite and investigated dislocation structures by TEM. A similar study was conducted by Thurel and Cordier (2003) and Thurel et al. (2003) who investigated the dislocation structures in more detail. However, no quantitative rheological data is available from these studies. Chen et al. (1998) conducted deformation experiments of wadsleyite and reported that wadsleyite is significantly stronger than olivine and that water has only a slight weakening effect on wadsleyite. However, for the following reasons their results may not be conclusive. First, their experiments were conducted at low temperature and pressure ($T < 900$ K, $P < 10$ GPa) compared to the typical conditions of wadsleyite-dominant region in the transition zone in Earth ($P = 13$–18 GPa and $T \sim 1800$ K) (e.g. Akaogi et al., 1989). Second and more importantly, their experiments are on powder samples and the stress was measured by X-ray peak broadening. In the deforming powder sample, effects of crushing, sintering and creep are considered to be combined, however, its physical mechanisms are poorly known. Therefore their results may not be relevant to high-temperature rheology of a dense material. Moreover, Kubo et al. (1998) studied the kinetics of olivine to wadsleyite transformation at $P = 13.5$ GPa and $T = 1300$ K, and inferred that water significantly enhances plastic deformation of wadsleyite. Consequently, we conclude that very little is known on the rheological properties of wadsleyite from previous studies.

* Corresponding author. Present address: Department of Earth and Planetary Sciences, Tokyo Institute of Technology, Meguro-ku, Tokyo 152-8551, Japan.
Tel.: +81 3 5734 2342; fax: +81 3 5734 3538.
E-mail address: yuu@geo.titech.ac.jp (Y. Nishihara).

0031-9201/$ – see front matter © 2008 Elsevier B.V. All rights reserved.
doi:10.1016/j.pepi.2008.03.003

The rheological property of olivine at relatively low pressure have been established based on many deformation experiments (e.g. Karato et al., 1986; Mei and Kohlstedt, 2000a, b; Karato and Jung, 2003). By contrast, the rheological properties of olivine at high pressure are still controversial. Using a liquid-cell Griggs apparatus, Green and Borch (1987) obtained a very large pressure effect corresponding to an activation volume of $V^* \sim 27\,cm^3$/mol. Based on the stress relaxation tests using the Kawai-type multi-anvil apparatuses up to $P = 15$ GPa, Karato and Rubie (1997) observed a significant pressure effect for dislocation creep of olivine yielding $V^* \sim 14\,cm^3$/mol after the correction for the water fugacity effect. Karato and Jung (2003) made a detailed analysis of pressure effects on dislocation creep in olivine based on the experimental data to $P = 2$ GPa under "wet" (water-saturated) conditions, and determined $V^* \sim 24\,cm^3$/mol after the correction for the water fugacity effect. In contrast, Li et al. (2006a) concluded that pressure has very small effect on the plastic strength of olivine in the dislocation creep regime based on their deformation experiments using the deformation-DIA apparatus up to $P = 10$ GPa and $T = 1500$ K. This conclusion is inconsistent with most of previous studies.

The main reason for the controversy over the rheology of wadsleyite and olivine is the difficulty in performing quantitative deformation experiments at high pressures. Conventional deformation apparatus such as the Griggs or the Paterson apparatus can be operated only at low pressures ($P < 3$ GPa or $P < 0.5$ GPa, respectively). Recently, the deformation-DIA (D-DIA) was developed and has been used up to ~10 GPa and ~1500 K (e.g. Wang et al., 2003; Li et al., 2006a). However, by using D-DIA, in which a cubic pressure medium is compressed by six anvils, it is still difficult to conduct deformation experiments at pressures above 10 GPa because of its anvil geometry. Yamazaki and Karato (2001) designed the rotational Drickamer apparatus (RDA) in which deformation experiments can be performed to large strain in simple shear geometry. Since anvils are better supported in this design, deformation experiments can be performed at significantly higher pressures than the D-DIA. Modifications to the sample assembly have been made and this apparatus has been operated at a synchrotron facility at high temperature and pressure by Xu et al. (2005). In this paper, we report the results of the first mechanical tests of wadsleyite under the transition zone conditions ($P \sim 16$ GPa and $T = 1600$ and 1800 K), and new high-pressure results of olivine at $P \sim 11$ GPa and $T = 1800$ K.

2. Experimental techniques

2.1. Sample preparation and characterization

A wadsleyite sample was synthesized from San Carlos olivine powder at $P = 15$ GPa and $T \sim 1400$ K for 1 h and an olivine sample was hot-pressed from San Carlos olivine powder at $P = 4$ GPa and $T = 1373$ K for 2 h using the KIWI 1000-t Kawai-type multi-anvil apparatus installed at Yale University. In these synthesis experiments, a powder sample was packed into a Mo foil capsule to keep constant oxygen fugacity. More details on the technique of the multi-anvil experiments are described elsewhere (Nishihara et al., 2006).

The samples show near-equilibrium textures (Fig. 1). The average grain size is 3.3 μm for wadsleyite and 4.6 μm for olivine. The average grain size was measured using linear intercept method with a stereographic correction factor of 1.5. The water content of the synthetic wadsleyite and olivine starting material is determined to be 20,000–30,000 and 2500 H/10^6 Si, respectively (Table 1) by using Fourier-transform infrared spectrometer (see later section for technical details). For $(Mg_{0.9}Fe_{0.1})_2SiO_4$ wadsleyite and olivine, the relationship between values of C_{OH} (H/10^6 Si), C_{H_2O} (wt.% H_2O) and C_{H_2O} (wt. ppm H_2O) can be approximated as follows; C_{OH} (H/10^6 Si) $= 16 \times 10^4 \times C_{H_2O}$ (wt.% H_2O) $= 16 \times C_{H_2O}$ (wt. ppm H_2O).

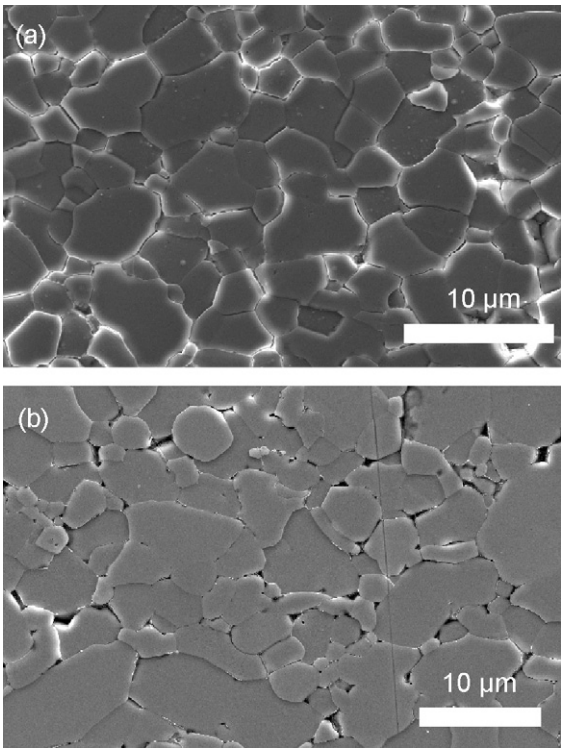

Fig. 1. SEM images of starting material (a) wadsleyite and (b) olivine. The starting materials show near-equilibrium texture.

2.2. Sample assembly

For deformation experiments with the RDA, we used a pair of tungsten-carbide anvils with 4.0 mm truncation diameter and

Table 1
Conditions of deformation experiments and results

	Wadsleyite		Olivine
	Bet24[a]	Bet25[a]	San84[a]
P (GPa)	15.2–15.8	15.3–17.6	9.9–12.1
T (K)	1600 ± 100	1800 ± 100	1800 ± 100
$d\phi/dt$ (° min^{-1})	0.098	0.101	0.103
During steady-state deformation			
$\dot{\varepsilon}_E$(10^{-5} s^{-1})	5.2 ± 2.0[b]	5.1 ± 1.9	6.6 ± 2.0
σ_E (GPa)	3.3 ± 0.3[c]	3.6 ± 0.6[c]	1.8 ± 0.2[c]
Max deformation			
t (min)	208	167	189
ϕ (°)	20.4	16.8	19.3
γ_a	0.94[b]	0.68	0.91
C_{OH} (H/10^6Si)			
Before	~20,000	27,000	2500
After	4000–7000	<1500[d]	<50[e]

[a] Run #.
[b] Estimated based on results in Bet25. See text for more details.
[c] Presented errors are from variation of equivalent stress during steady-state deformation.
[d] IR absorbance was detected only from limited part of sample. Generally no IR absorbance (<50 H/10^6 Si).
[e] No IR absorption is detected in the OH vibration region.

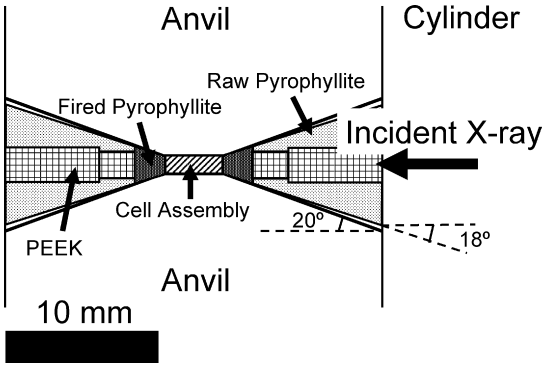

Fig. 2. Schematic illustration of gasket and surrounding parts used in Bet25 and San84.

20° slope (Fig. 2). A composite gasket made of pyrophyllite (raw and fired) and polyether ether ketone (PEEK) was employed. PEEK, which has low X-ray absorption, was placed in the X-ray paths. We used a slightly smaller angle (18–19°) for the gasket slope than that for the anvil (20°) to achieve more efficient pressure generation. In order to minimize absorption of X-ray, we used a sleeve (anvil holder) made of extra-super-duralumin (Al-alloy with Zn), which is nearly transparent to high energy X-rays (Xu et al., 2005).

A schematic drawing of cell assembly is shown in Fig. 3. A pair of disc heaters made of TiC + diamond composite is used within a pressure medium consisting of Al_2O_3, MgO and ZrO_2. The total thickness of the cell assembly is 1.0 or 1.2 mm. In order to minimize the stress gradient within a sample during deformation a ring-shaped wadsleyite sample was used. The sample is 0.4 mm thick with ~1.6 mm outer diameter and 1.0 mm inner diameter. A thin metal foil with a dimension of 200 μm × 200 μm was placed as a strain marker in a cut section of the ring-shaped sample (Fig. 3). A 25 μm thick Re foil was used in Bet 24 and 6 μm thick Mo foils were used in Bet 25 and San84. The central electrode is made of sintered TiC. In San84, the inner portion (0.7 mm wide) of MgO ring sample holder was replaced by Al_2O_3 ring.

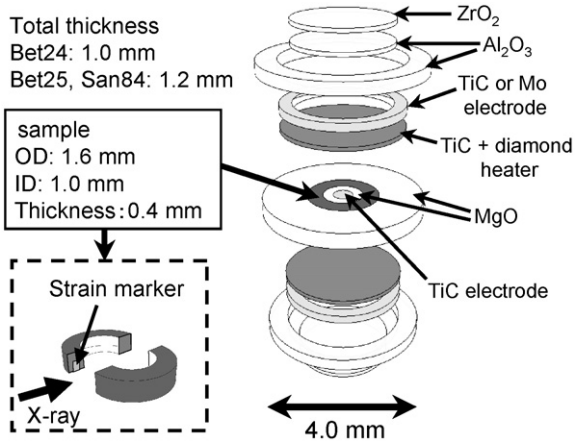

Fig. 3. Cell assembly used in the RDA high-pressure deformation experiments with conjunction of synchrotron radiation. Slightly different assembly design was used in Bet 24 and in Bet25 and San84. In Bet24 (Bet25 and San84), total thickness of the assembly was 1.0 mm (1.2 mm), an electrode ring was Mo (TiC), and strain markers were 25 μm thick Re foil (6 μm thick Mo foil). The difference of total thickness comes from different thickness of Al_2O_3 ring and disc and ring electrode in these two assembly.

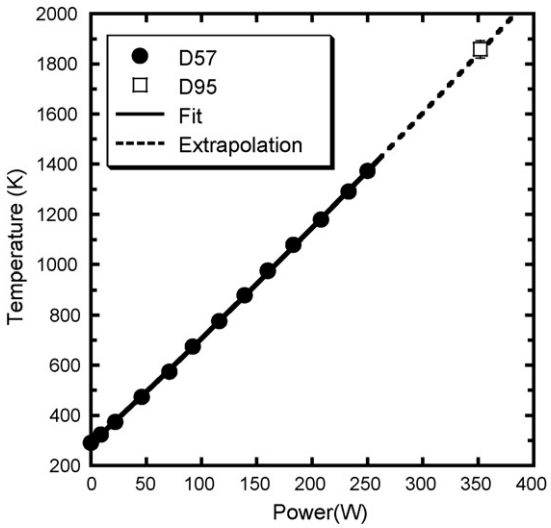

Fig. 4. Results of temperature calibration experiments. In D57, temperature was measured by using Pt–Pt10Rh thermocouple and measurements were failed above T = 1400 K. In D95, temperature at electric power of 352 W was determined from chemical composition of Ca-rich pyroxene coexisting with Ca-poor pyroxne in the system $Mg_2Si_2O_6$–$CaMgSi_2O_6$ (Gasparik, 1996). Power–temperature relationships in both experiments are consistent. Pressure conditions of these experiments are P = 12 GPa (D57) and 11 GPa (D95).

Temperature is estimated from the electric power based on a calibration performed in off-line experiments. The temperature calibration experiments were performed by two different techniques. In the first temperature calibration (D57), temperature was monitored using Pt–Pt10Rh thermocouple (made of 50 μm thick foils) with a sample assembly similar to that presented in our previous paper (Fig. 2a of Xu et al., 2005). In another temperature calibration (D95), temperature at constant electric power was determined by using pyroxene thermometry in the system $Mg_2Si_2O_6$–$MgCaSi_2O_6$ (e.g. Gasparik, 1990, 1996) using the same cell assembly as synchrotron experiments (Fig. 3). A sintered mixture of enstatite and diopside was used for the starting material. Although the experiment using thermocouple (D57) allows us to measure temperature *in situ*, temperature variation in the sample cannot be determined and any possible effects of thermocouple foils, which are good thermal conductors, on the power–temperature relationship cannot be evaluated. On the other hand, by the experiment using pyroxene thermometry (D95), temperature variation in sample can be determined using exactly the same assembly as synchrotron experiments. Pressure conditions of these experiments are P = 12 GPa (D57) and 11 GPa (D95). Fig. 4 shows power–temperature relationship determined by the calibration experiments. From D57, only the data below T = 1400 K were obtained due to thermocouple failure. In D95, sample was kept at high temperature with constant electric power of 352 W for 15 h. Chemical composition of Ca-rich pyroxene coexisting with Ca-poor pyroxene (high-pressure clinopyroxene) was measured using an electron microprobe. The chemical analysis of Ca-rich pyroxene in the entire area of the polished section in the recovered sample yielded X_{Di} = 0.70–076 (X_{Di} is molar content of $CaMgSi_2O_6$). Using this result, based on thermodynamic parameters reported by Gasparik (1996), temperature is calculated to be T = 1820–1890 K which indicate very small temperature variation (<100 K) within the sample. As is clear from Fig. 4, the power–temperature relationship is generally consistent between D57 and 95 suggesting good reproducibility of temperature generation. Based on the temperature calibration described above, we consider the uncertainty of temperature in this study to be about ±100 K.

2.3. Deformation experiments in conjunction with synchrotron radiation

A deformation experiment with the RDA is performed as follows. In Bet24 and 25, first a sample is first compressed to the target pressure ($P \sim 16$ GPa) at room temperature. During this process significant deformation occurs in the sample as well as surrounding materials. Then temperature is raised to $T = 1600$ or 1800 K. In San84, temperature was increased before the target pressure ($P \sim 11$ GPa) was reached. Since some pressure drop occurs during heating, it was difficult to estimate pressure at high temperature ($T > 1500$ K) accurately prior to heating. Heating during compression is a useful way to achieve exact target pressure at high temperature. A sample was kept at 1600 or 1800 K for 0.5–1 h to anneal the defects formed by cold deformation. After annealing, rotation of the top anvil is begun by turning on the motor with a constant rate of rotation. After rotation to a certain angle ϕ is completed, the motor is turned off and the heater current was shut off. Both stress and strain (displacement) in a sample space were monitored *in situ*. Three deformation experiments were carried out at the same rate of anvil rotation ($\sim 0.10^\circ$ min^{-1}), and their conditions are summarized in Table 1.

In situ observation of stress and strain was carried out using synchrotron radiation at Brookhaven National Laboratory, National Synchrotron Light Source (NSLS), X17B2 (Chen et al., 2004; Li et al., 2004a). Strain measurements were performed using X-ray radiographic images. The X-ray radiographs were collected using a CCD camera and a YAG scintillator with wide incident X-ray beam (2 mm × 2 mm).

Stress measurements were performed by X-ray diffraction with white X-ray. A 13-element solid-state detector was used to record the energy-dispersive X-ray diffraction patterns. The incident beam was collimated to 50 μm × 50 μm. The diffracted X-rays were collimated by using a conical slit (50 μm gap) and detected on four of the 13 detector elements (top, bottom and two side elements). By changing position of the detector spatially, X-ray diffraction pattern was collected at six different Ψ angles, $\Psi = 0^\circ$, $\pm 45^\circ$, $\pm 90^\circ$ and 180° (see Fig. 5). ^{57}Co γ-rays (14 and 122 keV) and characteristic X-rays of Pb ($K\alpha_1$ and $K\alpha_2$) were used for the energy calibration. The diffraction angle 2θ, which was mechanically fixed by the geometry of the conical slit, is $\sim 6.5^\circ$ and calibrated using a standard material (Al_2O_3 powder). The alignment of the sample is critical in this type of experiment. X-rays must be collected from one side of a sample along the central line in order to determine the stress (see Fig. 5) (Xu et al., 2005). A typical data collection time was 300–600 s. We measured the lattice spacing (d-spacing) of a sample as a function of orientation with respect to the compression direction.

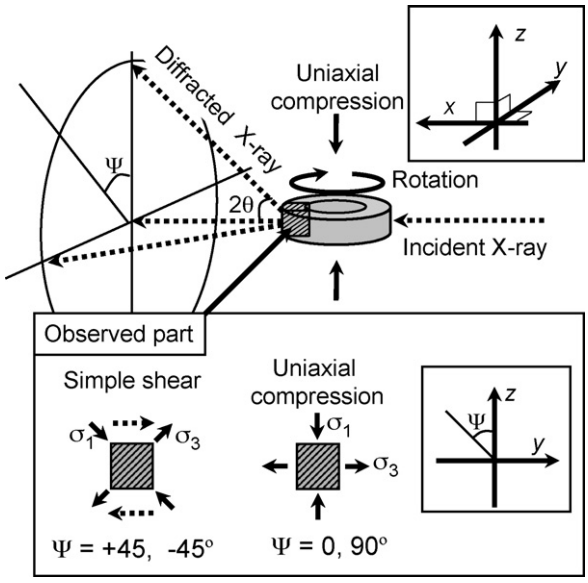

Fig. 5. Schematic illustration of X-ray diffraction geometry and state of deviatoric stress in the experiments. We take X-ray diffraction only from one part of ring-shaped sample (shaded area). In the observed area, state of deviatoric stress can be simplified to be a combination of shear and uniaxial stresses whose principal axes are in $\Psi = +45$ and -45° and in $\Psi = 0$ and 90°, respectively. σ_1 and σ_3 denote maximum and minimum principal stress axes, respectively. For simple shear and uniaxial compression, $\sigma_S = \sigma_1 - \sigma_3$ and $\sigma_U = \sigma_1 - \sigma_3$, respectively.

2.4. Strain measurements

The development of sample strain was monitored by X-ray radiograph of a strain marker (Mo or Re foil) which is observed in the images (Fig. 6). This enables *in situ* determination of sample strain (and strain rate). Because deformation in the RDA generally involves both uniaxial compression and simple shear, the geometry of strain marker is affected by these two components of deformation (Fig. 7). Thus strain (and strain rate) corresponding to both

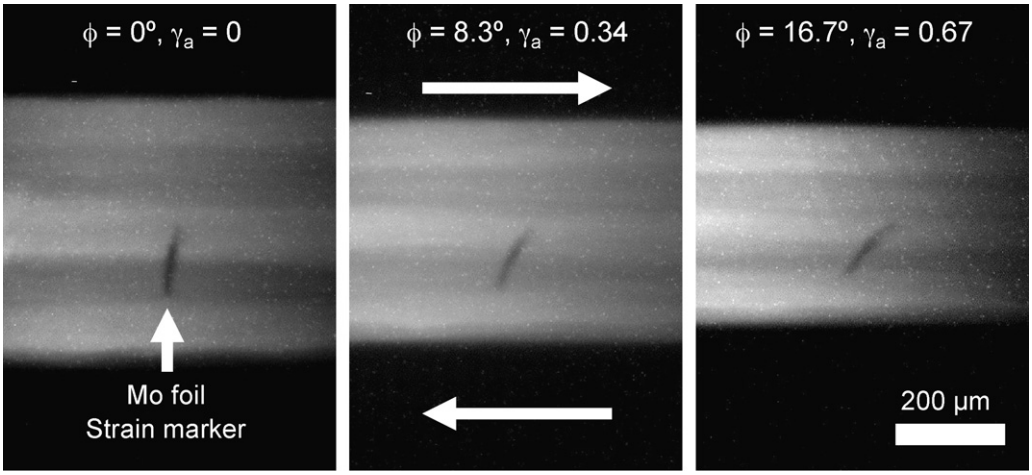

Fig. 6. Sample X-ray radiographs at $P \sim 16$ GPa and $T = 1800$ K in Bet25. (Left) before rotational deformation ($\phi = 0^\circ$, where ϕ is rotation angle), during deformation (center) at $\phi = 8.3^\circ$ and (right) $\phi = 16.7^\circ$. Deformation of sample is clearly recognized from tilt of Mo foil strain maker (black lines). Top and bottom black areas are anvils, and two dark gray layers within a sample are TiC + diamond heater.

uniaxial compression and simple shear have to be evaluated for accurate characterization of strain state.

A new formulation is developed to analyze strain state in the deforming sample and its details are described in the Appendix A. In the analysis, a theoretical equation was fit to observation of apparent sample strain γ_a which is defined as

$$\gamma_a \equiv \frac{w}{h} = \tan\alpha \tag{1}$$

where w, h and α are width and height of strain marker and tilt angle of strain marker, respectively (Fig. 7). The influence of uniaxial compression was taken in account based on the observed change of sample thickness before and after deformation experiments.

By the strain analysis, two independent components of strain rate tensor $\dot{\varepsilon}_U$ and $\dot{\varepsilon}_S$, strain rates corresponding to uniaxial compression and shear deformation, respectively, were determined. From $\dot{\varepsilon}_U$ and $\dot{\varepsilon}_S$, the equivalent strain rate $\dot{\varepsilon}_E$ was calculated for appropriate comparison with previous data which were taken in different deformation geometry. In the geometry of our deformation experiments, the equivalent strain rate $\dot{\varepsilon}_E$ is expressed as

$$\dot{\varepsilon}_E = \sqrt{\dot{\varepsilon}_U^2 + \frac{4}{3}\dot{\varepsilon}_S^2}. \tag{2}$$

The equivalent strain, $\dot{\varepsilon}_E$, and corresponding equivalent stress σ_E (defined later), can be used to characterize the rheological properties, if a material is plastically isotropic.

2.5. Stress and pressure measurements

Unlike D-DIA apparatus, the stress state of a sample in the RDA can be more complicated. With the assumption that the material motion occurs parallel and normal to the compression axis (for pressurization) and/or parallel to the rotation direction (for torsion), the deviatoric stress state in a sample ("observed part" in Fig. 5) can be simplified to a combination of two deviatoric stress components as

$$\sigma_{ij} = \begin{pmatrix} \frac{\sigma_U}{3} & 0 & 0 \\ 0 & \frac{\sigma_U}{3} & 0 \\ 0 & 0 & -\frac{2\sigma_U}{3} \end{pmatrix} + \begin{pmatrix} 0 & 0 & 0 \\ 0 & 0 & \frac{\sigma_S}{2} \\ 0 & \frac{\sigma_S}{2} & 0 \end{pmatrix} = \begin{pmatrix} \frac{\sigma_U}{3} & 0 & 0 \\ 0 & \frac{\sigma_U}{3} & \frac{\sigma_S}{2} \\ 0 & \frac{\sigma_S}{2} & -\frac{2\sigma_U}{3} \end{pmatrix} \tag{3}$$

where the z-axis (three-axis) is the compression direction (the rotational axis), the y-axis (two-axis) is the shear direction and the x-axis (one-axis) is normal to both of them (see Fig. 5) and σ_U and σ_S represent the two deviatoric stress components, respectively. The signs of diagonal components are chosen to yield a positive σ_U value for compression. Note that shear stress τ used in some previous studies is expressed as $\tau = \sigma_S/2$. In this case, the variation in d-spacing with orientation, $d_{hkl}(\Psi)$ is given by

$$d_{hkl}(\Psi) = d^0_{hkl}\left\{1 + \frac{\sigma_U}{6M}(1 - 3\cos^2\Psi) - \frac{\sigma_S}{2M}\sin\Psi\cos\Psi\right\} \tag{4}$$

where d^0_{hkl} is the d-spacing corresponding to the hydrostatic stress, Ψ is the orientation of a plane normal to a specific lattice plane relative to the orientation of compression (Fig. 5), M is an appropriate elastic (shear) modulus which depends on the crystallographic orientation of the plane (hkl) (e.g. Singh et al., 1998). Therefore from the measurements of Ψ dependence of d-spacing we can determine

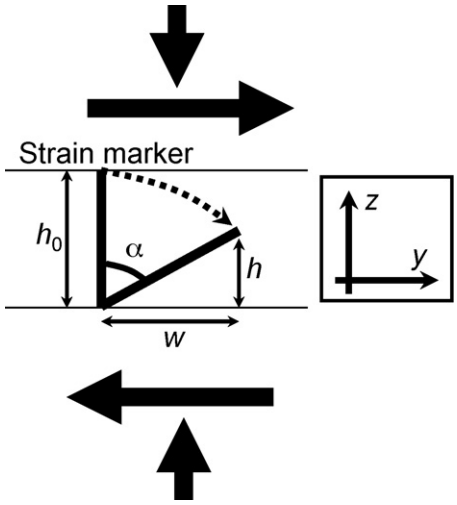

Fig. 7. Schematic illustration of deformation of strain marker (thick lines). Deformation of strain marker is affected by both simple shear and uniaxial compression (bold arrows). Height h and width w of strain marker change by deformation of sample while initial values are $h = h_0$ and $w = 0$ (at $t = 0$, where t is time after rotation started).

both σ_U and σ_S. We ignore any small difference between detector orientation (Ψ) and relevant crystallographic orientation which is smaller than $\theta = 3.25^\circ$. Eq. (4) contains three unknowns to be determined (d^0_{hkl}, σ_U and σ_S). Therefore we need to have a data set from at least three different Ψ angles.

Most of previous deformation experiments were performed in geometry of uniaxial compression. For appropriate comparison with those previous data, we use equivalent stress σ_E. In the geometry of our deformation experiments, the equivalent stress σ_E is expressed as

$$\sigma_E = \sqrt{3I_2} = \sqrt{\sigma_U^2 + \frac{3}{4}\sigma_S^2}, \tag{5}$$

where I_2 is the second stress invariant.

For simple shear deformation, the maximum (or minimum) stress occurs at $\Psi = \pm 45^\circ$ whereas for uniaxial compression, the maximum (or minimum) occurs at $\Psi = 0$ and $\pm 90^\circ$ (Fig. 5). Consequently, d-spacing shows extremes at these particular angles when only one of these stress systems is present. In real case, where both stress systems are present, the positions of extremes in d-sapcing change depending on the ratio of magnitudes of two deviatoric stress components.

In the present study, the (2 4 0) peak of wadsleyite and the (1 3 0) peak of olivine were the only diffraction lines observed throughout a series of experiments without any serious overlapping with other peaks. Therefore, we used the variation of d_{240} of wadsleyite and d_{130} of olivine to determine pressure and deviatoric stresses. Hydrostatic pressure P was determined from the value of d^0_{hkl} using an available data on the unit cell parameters as a function of P and T using an appropriate equation of state (Table 2).

The choice of M can be debated. We used the aggregate shear elastic modulus obtained experimentally (Table 2). In an elastically deformed material, the effective shear moduli M can be calculated using single crystal elasticity data (Singh et al., 1998). For the both (2 4 0) plane of wadsleyite at $P = 14$ GPa and the (1 3 0) plane of olivine at $P = 12$ GPa, the difference between aggregate shear modulus and M are <2% (Zha et al., 1997; Abramson et al., 1997). Therefore the choice of elastic constant does not affect the stress estimate very much if a sample deforms only elastically. In plastically deforming material, the actual value of M to be used here depends on

Table 2
Thermoelastic parameters

	Wadsleyite[a]	Olivine[b]
Parameters for P–T–d^3_{hkl} relationship[c]		
Index ($h\,k\,l$) of used d	2 4 0	1 3 0
K_{T0} (GPa)	189	113
K'_T	3.9	4.6
α_0 (10^{-5} K^{-1})	1.94	3.02
$(\partial K_T/\partial T)_V$ (GPa K^{-1})	[0]	[0]
$(\partial^2 P/\partial T^2)_V$ (10^{-7} GPa K^{-2})	17	8
Parameters for bulk shear modulus[d]		
G_0 (GPa)	107	78
G'	1.6	1.4
$(\partial G/\partial T)_P$ (GPa K^{-1})	−0.015	−0.014

[a] *References*: Suzuki et al. (1980), Fei et al. (1992), Jackson and Rigden (1996), Li and Liebermann (2000), Li et al. (2001), Inoue et al. (2004) and Mayama et al. (2004).
[b] *References*: Suzuki (1975), Isaak (1992), Guyot et al. (1996) and Abramson et al. (1997).
[c] Hydrostatic presure P was determined using P–T–d^3_{hkl} relationship expressed by a formulae of thermal equation of state combined with Birch-Murnaghan equation of state [Jackson and Rigden, 1996].
[d] Parameters for bulk shear moduls are for the equation, $G = G_0 + G'P + (\partial G/\partial T)_P T$.

the stress–strain distribution and is not very obvious. For further discussion on this issue, see Li et al. (2004b) and Weidner et al. (2004).

Some data on the distribution of stress in plastically deforming minerals are reported in previous studies using the D-DIA (Li et al., 2004b, 2006a,b). In deforming polycrystalline MgO at $P = 2.3$ and 4.5 GPa and $T = 773$ K, the calculated deviatoric stress differs significantly depending on the diffraction line selected, and calculated stress from (1 1 1) was higher than that from (2 0 0) by a factor of ∼2 (Li et al., 2004b). However, the stress heterogeneity is not quite serious for other silicate minerals. For pyrope garnet deforming at $P = 4.6$–6.8 GPa and $T = 1073$–1573 K, diffraction lines (4 0 0), (4 2 0), (3 3 2), (4 2 2) and (4 3 1) yielded quite consistent values of deviatoric stress with ranges within ±15% of the averaged value (Li et al., 2006b). For olivine deforming at $P = 3.5$–9.6 GPa and $T = 1073$–1473 K, calculated stress values from (0 2 1), (1 3 0), (1 3 1) and (1 1 2) diffraction lines typically range within ±30% of averaged value except for low stress data ($\sigma < 1$ GPa) for which resolution is relatively worse (Li et al., 2006a). For (1 3 0) of olivine, which is used in this study, the calculated stress value (σ_{130}) is generally larger than the averaged value (σ_{Ave}), and typically $\sigma_{130}/\sigma_{Ave} = 1.0$–1.4. On wadsleyite there is no similar report. In these studies, the average of stress values from several diffraction lines is assumed to be close to the effective stress for the bulk sample. Based on the previous data, the effective stress for olivine is considered to be between $0.5\sigma_{130}$ to $1.3\sigma_{130}$. For wadsleyite, we assume that the effective stress is between $0.5\sigma_{240}$ and $2\sigma_{240}$, where σ_{240} is calculated stress using a diffraction line (2 4 0).

To evaluate the uncertainties in stress estimate from X-ray diffraction, we have also determined the dislocation density in the olivine sample to estimate stress. Dislocation in the olivine samples were decorated at $T = 1123$ K for 1 h and observed by an SEM (Karato, 1987; Karato and Lee, 1999). The dislocation density versus stress relation determined by Karato and Jung (2003) is used to estimate the stress. The dislocation density–stress relationship is scaled using the pressure effects on elastic modulus and the Burgers vector to estimate the correction for the pressure effects. This correction is small (∼20%).

2.6. Microstructural and chemical analyses

Samples were examined using a Raman spectrometer for phase identification, and microstructures were observed using both optical and scanning electron microscopes (SEM). For the microstructural observation, polished sections of samples were etched by a mixture of HF, HNO_3 and acetic acid (1:1:1 in volume) (Wegner and Christie, 1985) for 5–30 s (wadsleyite) or a 37% hydrochloric acid for 6 min (olivine).

Water contents in the annealed sample were measured by a Fourier-transform infrared spectroscopy (FT-IR). For FT-IR measurements, samples were doubly polished to thickness of 15–190 μm depending upon water content. Samples were directly put on a KBr mount disk and analyzed with non-polarized IR beams with typical dimension of 40 μm × 40 μm. The water contents were calculated from background-subtracted absorbance spectra using the Paterson's (1982) calibration with appropriate correction for orientation factor (e.g. Kohlstedt et al., 1996).

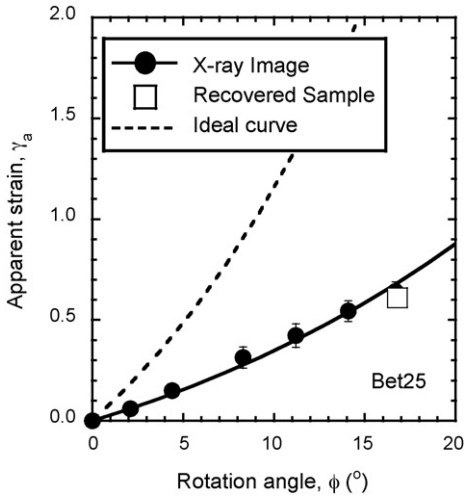

Fig. 8. Relationship between rotation angle of top anvil ϕ and apparent sample strain γ_a in Bet25. Solid circles represent data determined from X-ray images (e.g. Fig. 6). Open square is strain determined from geometry of strain marker in the recovered sample. Solid line is a fit of Eq. (A7). Ideal curve (dotted line) represents apparent sample strain expected when there is no shear deformation in pressure medium, which is calculated by $\gamma_a = \phi r/h$ (see text). Apparent strain at $\phi = 0°$ is adjusted to be $\gamma_a = 0$.

3. Results

3.1. Strain measurements

Strain marker was clearly observed by X-ray radiograph in a run Bet25 (Fig. 6). As shown in Fig. 8, apparent strain γ_a, which is determined from tilt angle of strain marker in the X-ray radiographs, increases monotonically with increasing rotation angle of anvil ϕ. An apparent strain γ_a determined from a recovered sample was consistent with that determined by X-ray image (Fig. 8). As a result of strain analyses (Section 2.4 and Appendix A), the $\dot{\varepsilon}_U$ and $\partial w/\partial t$ were determined to be $(3.9 \pm 1.8) \times 10^{-5}$ s^{-1} and $(4.0 \pm 0.1) \times 10^{-9}$ m s^{-1}, respectively, using strain marker height ($h = 58 \pm 5$ μm) derived from thickness of recovered sample. The result of a fit is also shown in Fig. 8 as a solid line.

Due to deformation of pressure medium, which mostly consists of Al_2O_3 (Fig. 3), whole anvil rotation was not transmitted to sample. We calculated the evolution of apparent strain γ_a for the ideal case in which whole anvil rotation is transmitted to sample deformation (Fig. 8). In the ideal case, apparent strain is expressed as $\gamma_a = \phi r/h$, where $r = r_0 \exp(\dot{\varepsilon}_U t/2)$ is mean radius of sample ring and r_0 is initial mean radius. The r_0 was determined to be ∼800 μm from mean radius of recovered sample in a testing experiments at $P \sim 15$ GPa with 10 min annealing at $T = 1800$ K without rotational deformation. The observed apparent strains γ_a are only 28–33%

of the ideal values suggesting relatively high plastic strength of wadsleyite.

It is noted that, even at a constant rotation rate of the anvil, the calculated shear strain rate $\dot{\varepsilon}_S$ (Eq. (A6)) gradually increased. This increase is because of sample thinning (uniaxial compression) during deformation. Therefore the equivalent strain rate $\dot{\varepsilon}_E$ (Eq. (2)) also slightly changed as a function of time. Fig. 9 shows calculated change of strain rates during deformation in Bet25 as a function of rotation angle, ϕ. The change of equivalent strain rate ($\dot{\varepsilon}_E$) during deformation is smaller than its estimated uncertainty. Thus when overall uncertainties are taken into account, deformation in Bet25 is considered to be carried out at nearly constant strain rate of $\dot{\varepsilon}_E = (5.1 \pm 1.9) \times 10^{-5}\,s^{-1}$ (Table 1).

Evolution of strain in San84 was analyzed by the same manner as described above for Bet25, and the $\dot{\varepsilon}_U$ and $\partial w/\partial t$ in San84 were determined to be $(5.5 \pm 1.6) \times 10^{-5}\,s^{-1}$ and $(3.7 \pm 0.3) \times 10^{-9}\,m\,s^{-1}$, respectively, using the strain marker height of the recovered sample ($h = 46 \pm 3\,\mu m$). In Bet24, radiograph of strain marker was not clear enough, and the sample strain in Bet24 was analyzed based on the results of Bet25. The $\dot{\varepsilon}_U$ and $\partial w/\partial\phi = (\partial w/\partial t)/(\partial\phi/\partial t)$ are assumed to be the same as those in Bet25. The equivalent strain rates $\dot{\varepsilon}_E$ during steady state deformation (see next section) are summarized in Table 1. We conclude that the three deforma-

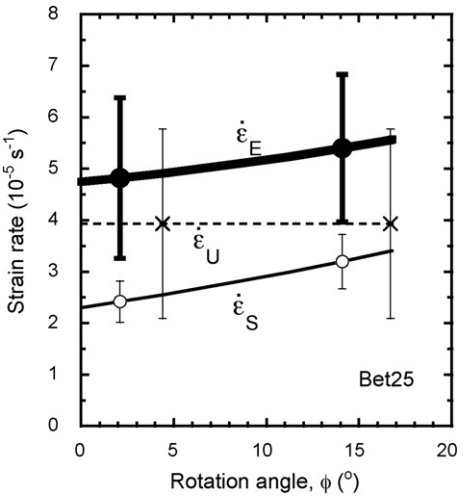

Fig. 9. Change of strain rates during deformation in Bet25 as a function of rotation angle, ϕ. Solid bold curve with solid circles, dashed line with crosses and solid thin curve with open circles are equivalent strain rate ($\dot{\varepsilon}_E$), uniaxial strain rate ($\dot{\varepsilon}_U$) and shear strain rate ($\dot{\varepsilon}_S$), respectively. Uncertainties are plotted as error bars with symbols.

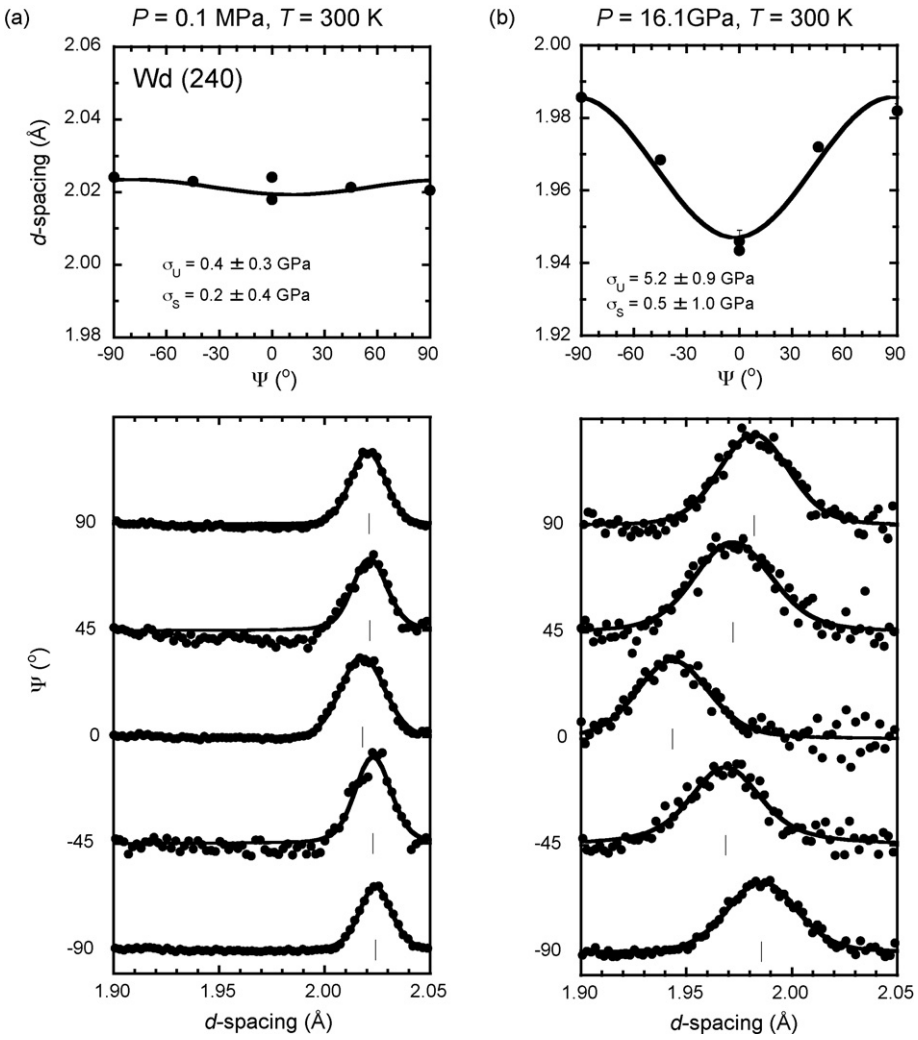

Fig. 10. Variations of wadsleyite (2 4 0) *d*-spacing as a function of Ψ angle in Bat24. (a) At $P = 0.1$ MPa and $T = 300$ K (before experiments), (b) at 16.1 GPa and 300 K (before heating), (c) at 15.9 GPa and 1600 K (before deformation), and (d) at 15.2 GPa and 1600 K during deformation. (Top column) *d*-spacing with fit of Eq. (4), (bottom column) X-ray diffraction pattern (background and neighboring peaks are subtracted). Presented errors for σ_U and σ_S are from misfit of Eq. (4).

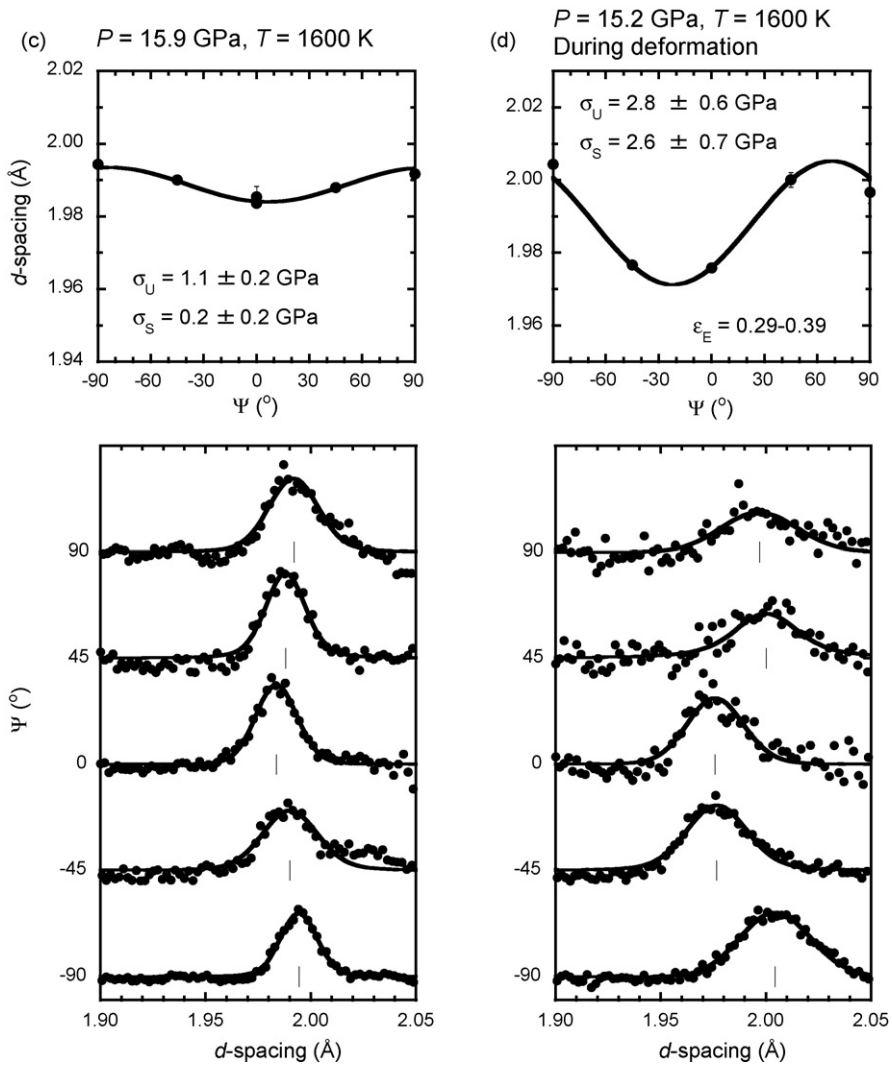

Fig. 10. (*Continued*).

tion experiments were performed at nearly identical strain rate, $\dot{\varepsilon}_E = 5–7 \times 10^{-5}\,s^{-1}$.

3.2. Stress measurements

Although three deformation experiments were conducted at constant press load, different behavior was observed in pressure during deformation for Bet24, and Bet25 and San84. Pressure was constant in Bet24 during high-temperature deformation (P = 15.2–15.8 GPa, Table 1). On the other hand, in Bet25 and San84, pressure increased slightly at initial stage of deformation ($\phi < \sim 7^\circ$ (Bet25) or $\sim 3^\circ$ (San84)) and, subsequently, decreased with increasing rotation angle of top anvil, ϕ. Consequently, pressure ranges during deformation are P = 15.3–17.6 and 9.9–12.1 GPa in Bet25 and San84, respectively (Table 1). This different behavior of pressure possibly comes from a difference in temperature. In Bet25 and San84, temperature during deformation is 200 K higher than that in Bet24. The higher temperature makes surrounding material softer, and this may affect stress (and pressure) distribution within the cell assembly during deformation. In the later section, in spite of some variations in pressure, we regard pressure conditions of the deformation experiments as nearly constant, $P \sim 16$ GPa for Bet24 and Bet25 and $P \sim 11$ GPa for San84.

Fig. 10 shows representative plots of d-spacing of wadsleyite (2 4 0) as a function of Ψ angle at various stages in the experiment Bet24. Before experiments, d-spacing is constant regardless of Ψ angle and deviatoric stresses (σ_U and σ_S) are zero within uncertainties (Fig. 10a). After pressurization to P = 16.1 GPa (before heating), the d-Ψ pattern shows strong variation showing large uniaxial stress (σ_U = 5.2 GPa) where d value at $\Psi = 0^\circ$ is significantly smaller than those at $\Psi = \pm 90^\circ$ (Fig. 10b). Note that the widths of diffraction peak at this condition are much broader than those before experiments probably due to microscopic stress heterogeneity. After heating to T = 1600 K at P = 15.9 GPa, the large uniaxial stress was significantly relaxed to be σ_U = 1.1 GPa (Fig. 10c). Here, the XRD peak widths are sharpened again. The d-Ψ pattern during rotational deformation is characterized by the deviation of principal stress axes (extremes of d-spacing) from $\Psi = 0$ and $\pm 90^\circ$ (Fig. 10d). In Fig. 10d, the minimum and maximum of d-spacing are located at $\Psi \sim -25$ and $\sim +65^\circ$, respectively, showing presence of significant shear and uniaxial stress components (σ_U = 2.8 GPa and σ_S = 2.6 GPa, respectively). The XRD peak widths during deformation are broader than those before rotation.

Figs. 11 and 12 show d-Ψ plots at several different strains during deformation in Bet25 and San84, respectively. As seen in these figures, with increasing strain, position of maximum and minimum of d-spacing shifts to lower Ψ-angle, and the amplitude of d-Ψ pat-

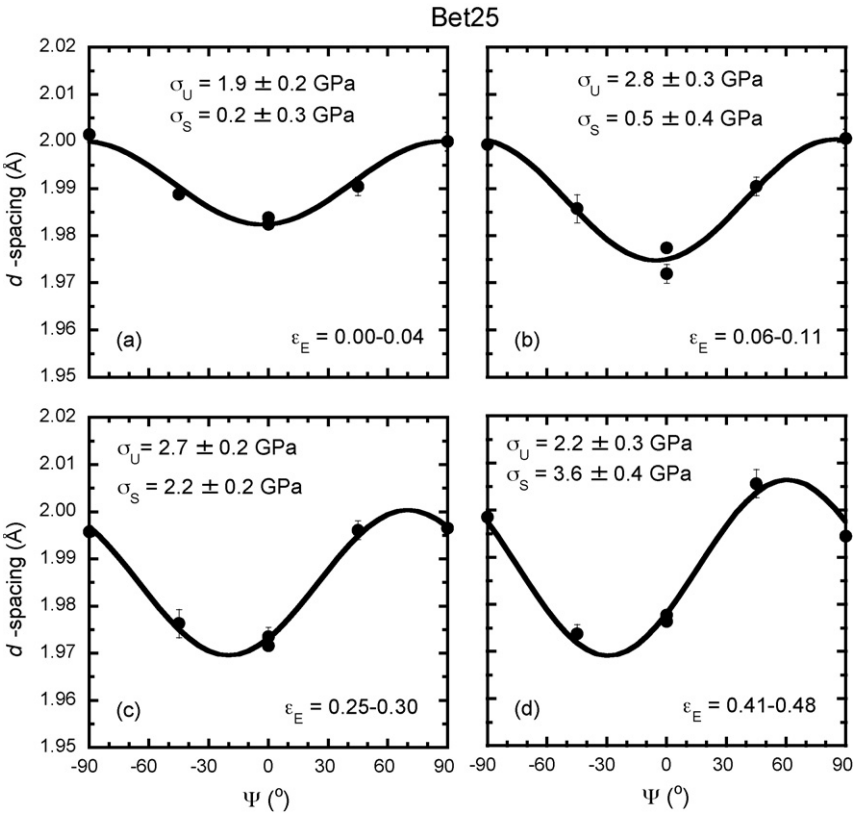

Fig. 11. Variations of wadsleyite (2 4 0) d-spacing as a function of Ψ angle during deformation at $P \sim 16$ GPa and $T = 1800$ K in Bet25, (A) at $\varepsilon_E = 0.00$–0.04, (b) at $\varepsilon_E = 0.06$–0.11, (c) at $\varepsilon_E = 0.25$–0.30, and (d) at $\varepsilon_E = 0.41$–0.48. Solid curves are fit of Eq. (4). Presented errors for σ_U and σ_S are from misfit of Eq. (4).

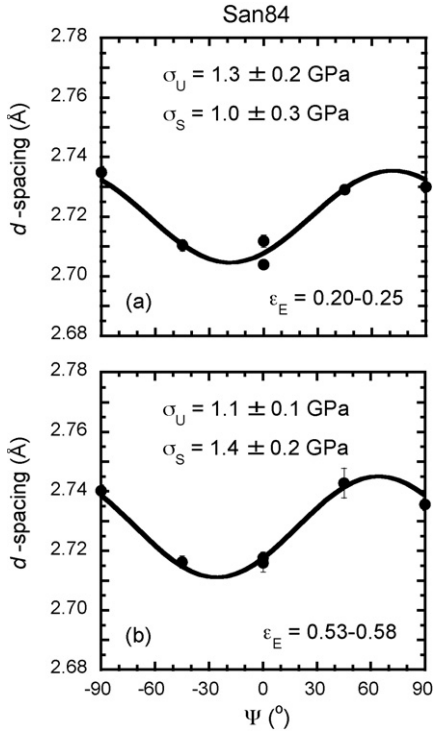

Fig. 12. Variations of olivine (1 3 0) d-spacing as a function of Ψ angle during deformation at $P \sim 11$ GPa and $T = 1800$ K in San84, (A) at $\varepsilon_E = 0.20$–0.25, (b) at $\varepsilon_E = 0.53$–0.58. Solid curves are fit of Eq. (4). Presented errors for σ_U and σ_S are from misfit of Eq. (4).

tern increases. This indicates the increase of shear stress σ_S during rotational deformation.

Fig. 13 shows evolution of uniaxial and shear stresses in the three experiments. Two experiments of wadsleyite at different temperature yielded similar magnitudes of deviatoric stresses in both σ_U and σ_S. On the other hand, the magnitude of deviatoric stresses for olivine are about half of those of wadsleyite. However, the qualitative variation of these stresses during deformation is similar for wadsleyite and olivine. Before rotational deformation started, shear stress σ_S was undetectably small while uniaxial stress σ_U was of some magnitude ($\sim$1–2 GPa). Although we observed a slight increase at the initial stage ($\varepsilon_E < 0.1$–0.2) and subsequent decrease in uniaxial stress σ_U, the σ_U is nearly constant through the deformation experiments. In contrast, the shear stress σ_S changed more significantly. At the initial stage of deformation ($\varepsilon_E < \sim 0.2$) the σ_S increased rapidly from $\sigma_S \sim 0$ GPa. After that, the increasing rate of σ_S became smaller as a function of strain ε_E.

Fig. 14 shows the variation of equivalent stress σ_E (Eq. (5)) as a function of equivalent strain ε_E at equivalent strain rate of $\dot{\varepsilon}_E \sim (6 \pm 1) \times 10^{-5}\ s^{-1}$. As mentioned above, the stress and strain states of samples in the RDA are complicated because of the significant contributions from two components of deformation (uniaxial compression and simple shear deformation). By using σ_E and ε_E (and $\dot{\varepsilon}_E$), stress and strain (and strain rate) are normalized to be comparable to uniaxial compression. In all three experiments, steady-state flow stress was achieved after deformation of $\varepsilon_E \sim 0.2$. The flow stress was $\sigma_E \sim 3.5$ GPa in two wadsleyite experiments at $P \sim 16$ GPa and $T = 1600$ and 1800 K, and $\sigma_E \sim 1.8$ GPa in olivine experiments at $P \sim 11$ GPa and $T = 1800$ K. These results are summarized in Table 1.

Equivalent stress and equivalent strain can characterize the plastic properties of material if plastic property is isotropic. To test the assumption of plastic isotropy, we use the Levy-von Mises relation

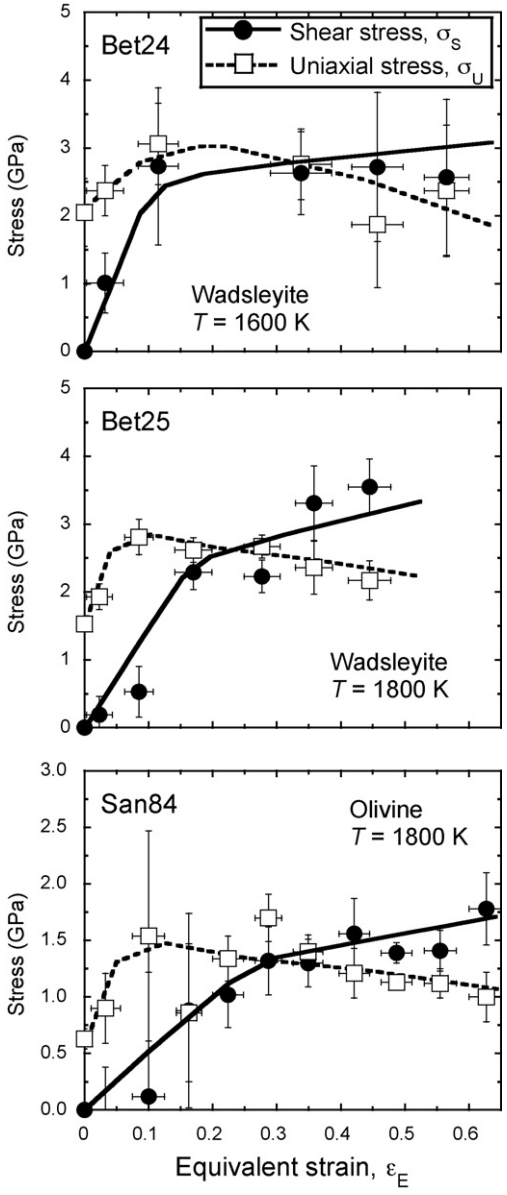

Fig. 13. Variation of uniaxial and shear stresses as a function of equivalent strain. Shear and uniaxial stresses are shown as solid circles with solid lines and open squares with broken lines, respectively. Equivalent strain rate is $\dot{\varepsilon}_E = (6 \pm 1) \times 10^{-5}\ s^{-1}$ in all the three experiments (Table 1). Presented errors for σ_U and σ_S are from misfit of Eq. (4).

(see e.g. Odqvist, 1974), viz.,

$$\dot{\varepsilon}_{ij} \propto (I_2)^{(n-1)/2}\sigma_{ij}, \tag{6}$$

where n is the stress exponent in power law creep equation. If this equation works (i.e. if the material is plastically isotropic), then we should have

$$\frac{\dot{\varepsilon}_U}{\dot{\varepsilon}_S} = -\frac{\dot{\varepsilon}_{zz}}{\dot{\varepsilon}_{yz}} = -\frac{\sigma_{zz}}{\sigma_{yz}} = \frac{4}{3}\frac{\sigma_U}{\sigma_S}. \tag{7}$$

For all three experiments, the ratios of strain rate calculated from $\sigma_U \approx \sigma_S$ (Fig. 13) is $\dot{\varepsilon}_U/\dot{\varepsilon}_S \sim 1.3$. This ratio is comparable to results calculated from strain rate observations, $\dot{\varepsilon}_U/\dot{\varepsilon}_S \sim 1.1$–$1.8$. This result indicates that the assumption of plastic isotropy is justifiable within experimental error.

The validity of stress measurements was also examined from dislocation density of olivine. This method is based on the well-known relationship between dislocation density and stress, $\rho b^2 = A(\sigma/G)^m$, where ρ is dislocation density, b is the length of the Burgers vector, A is a non-dimensional constant, σ is the differential stress, G is the shear modulus, and m is a constant. The dislocation density in olivine can be determined using a high-resolution SEM through a measurement of the total length of dislocations per unit volume [for details see (e.g., Karato, 1987; Karato and Lee, 1999; Karato and Jung, 2003)]. The physical basis for such a relation is the force balance, and the relation can be scaled to high pressure and temperature by using high-pressure values of b and G (Table 2). The results show $\sigma \sim 1.3$ GPa, which is in reasonable agreement with the results from X-ray diffraction (Fig. 14, Table 1).

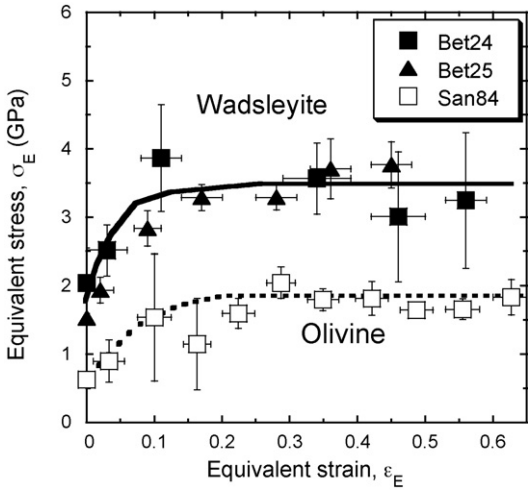

Fig. 14. Variation of equivalent stress σ_E as a function of equivalent strain ε_E. Equivalent strain rate is $\dot{\varepsilon}_E = (6 \pm 1) \times 10^{-5}\ s^{-1}$ in all the three experiments (Table 1). Presented errors for σ_E are propagated from misfit of Eq. (4).

3.3. Water content and microstructure

Fig. 15 compares representative FT-IR spectra of wadsleyite (a) before experiments (starting material) and after experiments (b) Bet24 and (c) Bet25 in OH vibration region. This figure shows that most of water in starting material escaped during deformation experiments at high temperature and high pressure. The initial modest water content ($C_{OH} \sim 20{,}000$–$30{,}000$ H/10^6 Si) was signifi-

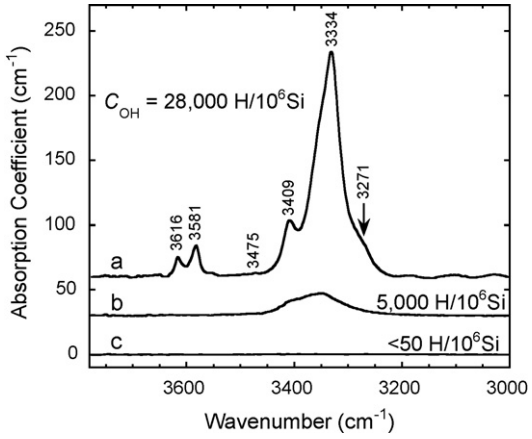

Fig. 15. Representative FT-IR spectra of wadsleyite (a) before experiments and after experiments (b) Bet24 and (c) Bet25. The water contents were heterogeneous within recovered samples (Bet24, Bet25), while those of starting material show homogeneous water distribution. Significant amount of water was escaped during experiments (Table 1).

cantly decreased to 4000–7000 (Bet24) and <1500 H/10^6 Si (Bet25) after experiments (Table 1). The more significant water escape in Bet25 is probably due to higher temperature. The water contents were heterogeneous within recovered samples, while those of starting material show homogeneous water distribution. Heterogeneous water distribution in a recovered sample is presumably due to temperature gradient in a sample.

The FT-IR pattern of starting material (Fig. 15a) consists of several sharp peaks at around ~3300 and ~3600 cm^{-1}, and it is very similar to previously reported patterns of wadsleyite with similar water content (e.g. Jacobsen et al., 2005; Nishihara et al., 2008). On the other hand, spectra of recovered samples (Fig. 15b) show only a spread peak at ~3350 cm^{-1}. Since the samples were quenched from high deviatoric stress conditions, crystal lattice of sample may be distorted even at room condition. This may be a reason of the spread IR peak.

For starting material of olivine, we observed FT-IR spectra which are similar to those of previous studies (e.g. Bai and Kohlstedt, 1993; Kohlstedt et al., 1996), and their water content was ~2500 H/10^6 Si. Since we used a polycrystalline sample, some amount of water may be stored at the grainboundaries (e.g. Karato et al., 1986). During deformation experiments San84, a significant amount of water escaped from the sample, and the water content in the recovered sample was undetectably small (<50 H/10^6 Si, Table 1).

Fig. 16 shows microstructure of recovered wadsleyite and olivine samples. The starting material showed equi-granular texture with average grain size of 3.3 μm for wadsleyite and 4.6 μm for olivine (Fig. 1). After deformation experiments, significant changes in microstructure were observed. For wadsleyite experiments, the recovered sample consists of two different types of grains: large elongated grains with grain size similar to that of starting material and surrounding small grains (<2 μm) (Fig. 16a and b). This texture is particularly clearer in the sample Bet25 (Fig. 16b). As reported previously (Xu et al., 2005), annealing of wadsleyite at similar condition (P = 15 GPa, T = 1700 K, t = 1 h) does not yield any change in microstructure from starting material. Thus we conclude that the observed microstructure in recovered wadsleyite samples (Bet24 and 25) was developed during deformation. The microstructure of deformed wadsleyite (Fig. 16a and b) suggests that dynamic recrystallization occurred in a localized portion of sample during deformation. On the other hand, grain size of recovered olivine sample (San84) was nearly homogeneous (3–7 μm). No significant difference was observed between grain size of starting material and that of the recovered sample (Figs. 1b and 15c).

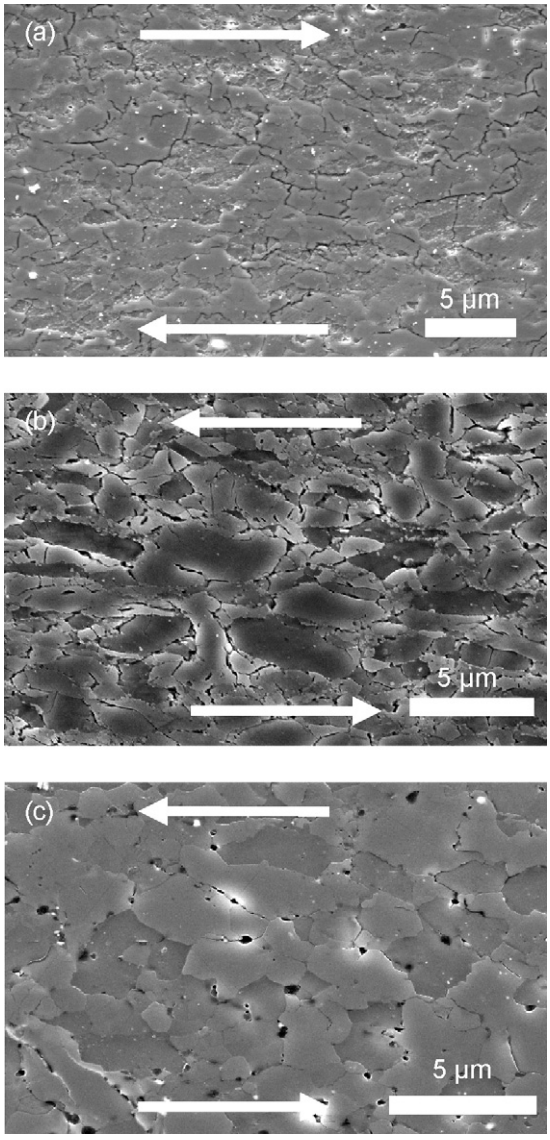

Fig. 16. SEM images of deformed samples. (a) Wadsleyite deformed at T = 1600 K (Bet24), (b) wadsleyite deformed at T = 1800 K (Bet25), and (c) olivine deformed at T = 1800 K (San84). The existence of smaller grains in recovered wadsleyite sample suggests occurrence of dynamic recrystallization during deformation.

4. Discussion

4.1. Strength of wadsleyite and olivine

Although our experimental studies have provided the first complete stress–strain curves to large strains showing both transient and steady-state behavior at P > 10 GPa, there are several enigmatic observations that need to be addressed before the details of the mechanical data can be interpreted.

First, the uniaxial stress on the sample is reduced by high temperature annealing, but it is increased during deformation and reached a nearly constant value at large strains (Fig. 13). We interpret this change is due to the reduction of effective viscosity of surrounding materials, such as MgO and pyrophyllite, due to their non-linear rheology. During rotational deformation, radial flow of the surrounding material could be enhanced compared to sample due to their non-linear rheology. Consequently, the uniaxial stress in the surrounding materials was preferentially relaxed, and, alternatively, the uniaxial stress in the sample increased. The radial flow of the surrounding material could be minimized by using stronger materials surrounding a sample. Despite this complication, we believe that our mechanical data are robust as far as the isotropy of rheological properties is justified, since our analysis include both uniaxial and shear components of stress and strain. The validity of the assumption of rheological isotropy is provided by our analysis discussed in the previous section.

Second, we observed almost the same magnitude of steady-state flow stress in Bet24 and 25. Temperature in Bet25 is 200 K higher than that in Bet24 whereas strain rate is nearly the same ($\dot{\varepsilon}_E \sim (6 \pm 1) \times 10^{-5}\ s^{-1}$). This difference is puzzling because the higher temperature usually makes material softer due to the thermal activation. As is widely known, widely, plastic strength of olivine is significantly reduced by the presence of water (e.g. Karato et al., 1986; Mei and Kohlstedt, 2000a,b; Karato and Jung, 2003). Water weakening is also suggested for wadsleyite from stress relaxation tests on anhydrous and hydrous wadsleyite at P = 10 GPa and T = 673–873 K (Chen et al., 1998) (see also Kubo et al., 1998). Thus

water content is considered to have significant influence on plastic strength in wadsleyite. As shown above, water content in the recovered sample is lower in Bet25 than that in Bet24 by more than factor of 2 (Table 1). Therefore the similar strengths of Bet24 and 25 could be attributed to a trade-off of temperature effect and water effect.

As shown above, quasi-steady state deformation was achieved at the later stage of all the three experiments (Fig. 14). If water content changed significantly during deformation, then steady-state deformation is unlikely to be achieved. Thus the change of water content in samples likely occurred prior to deformation, i.e. during annealing, and the water contents in the sample might be nearly constant at least at the later stage of deformation. From a comparison of the stress–strain curves of Bet25 and San84 (Fig. 14), we conclude that wadsleyite is stronger than olivine by factor of ~2 at $\dot{\varepsilon}_E \sim (6 \pm 1) \times 10^{-5}\ s^{-1}$, $T = 1800$ K and at relatively dry condition.

Not much can be said about the microscopic mechanisms of deformation from the present study. However, from the microstructural observations at the grain level, we conclude that deformation is due to dislocation motion. The key observations include (i) evidence of dynamic crystallization in wadsleyite that occur only when deformation is due to dislocation motion (Gottstein and Mecking, 1985) and (ii) a high density of dislocations (in olivine). This conclusion is in harmony with the all known experimental results on deformation of wadsleyite (Thurel and Cordier, 2003; Thurel et al., 2003) and olivine (e.g. Karato et al., 1986). In addition, we also note that appreciable lattice-preferred orientation is observed on wadsleyite deformed at similar condition (Xu et al., 2005) that also indicates the operation of dislocation creep (e.g., Van Houtte and Wagner, 1985).

4.2. Comparison with previous studies

We compare present mechanical data of wadsleyite and olivine with previous data on rheological properties in these minerals by dislocation creep (including power law and Peierls mechanisms).

Fig. 17 compares the creep strength of wadsleyite and olivine from this study with those from previous studies at relatively dry condition and (equivalent) strain rate of $\dot{\varepsilon} = 6 \times 10^{-5}\ s^{-1}$. Data for wadsleyite are from Chen et al. (1998) and data for olivine are from Evans and Goetze (1979), Karato and Jung (2003), Li et al. (2004a, 2006a) and Raterron et al. (2004). For this comparison, data from Li et al. (2004a, 2006a) were interpolated or extrapolated to $\dot{\varepsilon} = 6 \times 10^{-5}\ s^{-1}$ assuming power law equation $\dot{\varepsilon} \propto \sigma^n$ at each P–T condition. In this interpolation (or extrapolation), the stress exponent n was derived by fitting of the power law equation at each P–T condition. Data with large uncertainty were not used. We omitted data for which the estimated error of stress is larger than the absolute value of stress, and large extrapolations exceeding the range of data distribution in $\log_{10} \dot{\varepsilon}$ (at each P–T condition) was avoided. At $P = 0.1$ MPa and $\dot{\varepsilon} = 6 \times 10^{-5}\ s^{-1}$, the boundary between Peierls mechanism and power law creep is at $T = 1410$ K (Evans and Goetze, 1979; Karato and Jung, 2003).

Previous studies on deformation of olivine using D-DIA by Li et al. (2006a) reported that the effect of pressure on plastic strength is undetectably small. The small pressure effect on plastic strength of olivine is also reported in stress relaxation tests with synchrotron radiation (Raterron et al., 2004; Li et al., 2004a). On the contrary, our olivine data at $P \sim 11$ GPa showed significantly larger strength compared to the strength at $P = 0.1$ MPa. The large pressure effect on the creep strength is consistent with the previous results based on the results of stress relaxation tests at $P = 15$ GPa (Karato and Rubie, 1997; Karato and Jung, 2003), and such a large pressure effect is predicted by homologous temperature scaling (Karato, 1989). In Fig. 17, we show calculated stress of olivine at $P = 11$ GPa based on Karato and Jung (2003), which is largely consistent with the result of this study.

The reason for the large difference in the strength of olivine between these two sets of studies (one based on D-DIA and another based on RDA) is not well known. We could consider two possible reasons. First, the water content in the samples in these studies was different. Water content in olivine during deformation is estimated to be ~3000 H/10^6 Si in the D-DIA study (Li et al., 2006a). The water content in our sample (San84) is rather low (<50 H/10^6 Si), which could partly explain the discrepancy. Second, as our stress–strain curve indicates, a large equivalent strain ($\varepsilon_E \sim 0.2$) is needed to

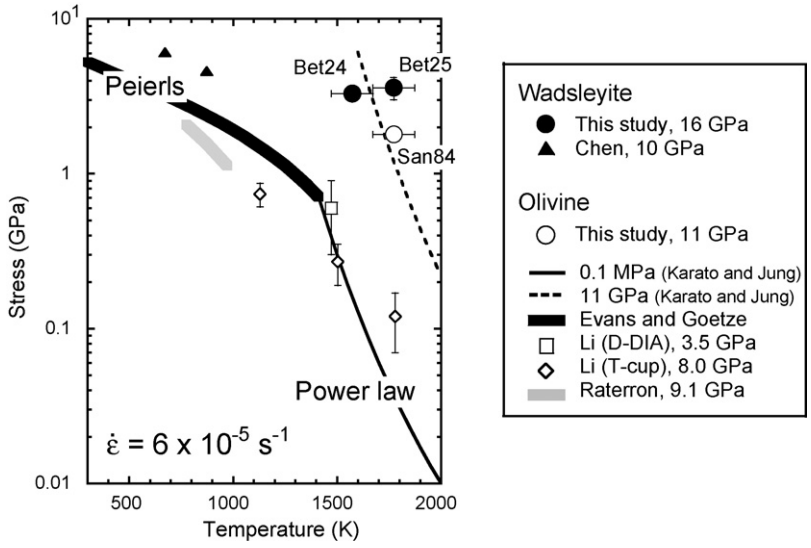

Fig. 17. Comparison of strength between wadsleyite and olivine at normalized strain rate of $\dot{\varepsilon} = 6 \times 10^{-5}\ s^{-1}$. Data for wadsleyite are from this study and Chen et al. (1998) (stress relaxation tests at 10 GPa). Data for olivine are from this study, Evans and Goetze (1979) (Peierls mechanism creep, indentation test at $P = 0.1$ MPa), Karato and Jung (2003) (power law creep), Li et al. (2006a) (D-DIA experiments at 3.5 GPa), Li et al. (2004a) (stress relaxation tests with T-cup at 8.0 GPa), and Raterron et al. (2004) (stress relaxation tests at 9.1 GPa). Our datum of olivine at $P \sim 11$ GPa is consistent with Karato and Jung (2003). Plastic strength of wadsleyite is higher than that of olivine. The error for data of this study is from variation of stress during steady-state deformation (Fig. 14) and does not includes uncertainty for stress distribution in deforming sample (see section 2.5).

achieve quasi-steady state deformation. However, only small strain ($\varepsilon_E < 0.05$) was imposed in D-DIA experiments by Li et al. (2006a) and stress relaxation tests with T-cup multi-anvil apparatus by Li et al. (2004a), while the magnitude of total strain is not clear in stress relaxation tests with the DIA apparatus by Raterron et al. (2004). Thus steady-state deformation is unlikely to be achieved in these previous experiments, which might have led to underestimates of the strength of olivine at high pressure and high temperature. Similarly, stress relaxation tests with DIA apparatus by Chen et al. (1998), in which the magnitude of strain is unclear, might underestimate the strength of wadsleyite.

4.3. Summary and conclusion

The present study has shown that quantitative rheological measurements can be performed under the pressure and temperature conditions equivalent to the transition zone conditions (up to $P \sim 16$ GPa, $T = 1800$ K) using the RDA. We have also tested the validity of X-ray diffraction measurement of stress by comparing the stress estimated from dislocation density (in olivine). The stress values from two independent estimates agree within the experimental uncertainties. This agreement is partly due to the absence of significant plastic anisotropy in olivine that has been demonstrated by the present study.

With the RDA, one can investigate the whole stress–strain curves to large strain to characterize the mechanical properties including the transient response as well as quasi-steady state behavior. At steady state, wadsleyite is somewhat stronger than olivine, and the creep strength of olivine at $P \sim 11$ GPa is considerably higher than those at lower pressures.

However, there are a number of issues that need to be improved to make this kind of measurements more useful. (1) The stress levels that we have observed are too high in comparison to what we expect in Earth. We need to increase temperature or reduce strain rate (or add water) to bring the stress level lower. (2) The geometry of deformation is not ideal. There is a significant contribution from uniaxial compression in addition to shear deformation. Improvements to sample assembly are needed to obtain better-defined deformation geometry. This is particularly critical to the study of deformation fabrics (lattice-preferred orientation). (3) Water content in our sample is not well controlled, and is rather small. A better way to control the water content needs to be developed. (4) The present paper reports results from only limited conditions. More data from a wide range of strain rates, temperature, pressure, grain size and water content will be needed to investigate the rheological behavior of Earth's deep mantle. For example, the rheological contrast across the actual 410-km discontinuity depends also on the contrast in water content. Under relatively "dry" conditions explored in the present study, wadsleyite is stronger than olivine, but a jump in water content at 410-km inferred by Huang et al. (2005) could counteract with this trend. The present work will form a basis for further more detailed studies on the rheological properties of Earth's deep interior.

Acknowledgements

The synchrotron experiments were carried out at National Synchrotron Light Source (NSLS) and technically supported by D.J. Weidner, M. Vaughan, L. Wang, C. Koleda and J. Chen. We thank I. Katayama, W. Landuyt, P.A. Skemer for their helpful support for the synchrotron experiments, Z. Jiang for support in SEM analyses and J. Hustoft for reading of the manuscript. We also thank two anonymous reviewers for constructive reviews. This research was partially supported by COMPRES, the Consortium for Materials Properties Research in Earth Sciences under NSF Cooperative Agreement EAR 01-35554. Y.N. is grateful for the Research Fellowships of the Japan Society of the Promotion of Science for Young Scientists.

Appendix A. Strain analyses

Deformation in the RDA involves both shear strain and uniaxial compression. Therefore in calculating the sample strain from the tilt of a strain marker (γ_a), the influence of thickness change necessarily must be taken into account for accurate evaluation of the strain rate. The sample strain is analyzed by the following procedure.

In our deformation geometry, the strain rate tensor can be written as

$$\dot{\varepsilon}_{ij} = \begin{pmatrix} \frac{\dot{\varepsilon}_U}{2} & 0 & 0 \\ 0 & \frac{\dot{\varepsilon}_U}{2} & \dot{\varepsilon}_S \\ 0 & \dot{\varepsilon}_S & -\dot{\varepsilon}_U \end{pmatrix} \tag{A1}$$

where $\dot{\varepsilon}_U$ and $\dot{\varepsilon}_S$ are uniaxial and shear strain rates, respectively. The relevant system of coordinates is shown in Fig. 5. The signs are chosen to yield positive values in $\dot{\varepsilon}_U$ and $\dot{\varepsilon}_S$ for positive σ_U and σ_S values (Eq. (3)), respectively. Note that the strain $\dot{\gamma}$ used in some previous shear deformation studies (e.g. Zhang et al., 2000) is expressed by $\dot{\gamma} = 2\dot{\varepsilon}_S$. The geometry of a strain marker is imaged by the X-ray radiography as a nearly linear image in the current sample geometry (Fig. 6). In this case, the orientation of a strain marker can be characterized by its height h and width w at time t (see Fig. 7). Since the height of the strain marker is half of the sample thickness (Fig. 3), h and w are regarded as halves of sample thickness and sample shear displacement, respectively. By using these parameters, $\dot{\varepsilon}_U$ and $\dot{\varepsilon}_S$ are given by

$$\dot{\varepsilon}_U = -\frac{1}{h}\frac{\partial h}{\partial t}, \tag{A2}$$

$$\dot{\varepsilon}_S = \frac{1}{2}\frac{1}{h}\frac{\partial w}{\partial t}. \tag{A3}$$

Because our experiments were carried out with a constant rate of anvil rotation, we assume $\partial w/\partial t$ to be constant. According to our off-line experiments, sample thickness is found to be shortened with increasing rotation angle up to $\phi = 40^\circ$ with nearly constant rate (unpublished data by Xu). Since our experiments were carried out at a constant rate of anvil rotation, we also assume $\dot{\varepsilon}_U$ to be constant with time t. From this assumption, h was derived to be

$$h = h_0 \exp(-\dot{\varepsilon}_U t), \tag{A4}$$

where h_0 is initial height of strain marker (Fig. 7). Hence, shear strain ε_S, shear strain rate $\dot{\varepsilon}_S$ and apparent strain γ_a can be expressed as a function of time t as

$$\varepsilon_S = \frac{1}{2\dot{\varepsilon}_U h_0}\frac{\partial w}{\partial t}\{\exp(\dot{\varepsilon}_U t) - 1\}, \tag{A5}$$

$$\dot{\varepsilon}_S = \frac{1}{2h_0}\frac{\partial w}{\partial t}\exp(\dot{\varepsilon}_U t), \tag{A6}$$

$$\gamma_a = \frac{w}{h} = \frac{t}{h_0}\frac{\partial w}{\partial t}\exp(\dot{\varepsilon}_U t). \tag{A7}$$

Note that this analysis does not require any information of stress state.

In the analysis, three parameters, h_0, $\dot{\varepsilon}_U$ and $\partial w/\partial t$, are required for complete description of sample deformation. The h_0 was determined to be 86 ± 14 μm from thickness of recovered sample in a testing experiments at $P \sim 15$ GPa with 10 min annealing at $T = 1800$ K without rotational deformation. The $\dot{\varepsilon}_U$ was determined

using thickness of a recovered sample (Eq. (A4)). Finally, $\partial w/\partial t$ was determined by a fit of Eq. (A7) to the *in situ* data of apparent strain γ_a.

References

Abramson, E.H., Brown, J.M., Slutsky, L.J., Zaug, J., 1997. The elastic constants of San Carlos olivine to 17 GPa. J. Geophys. Res. 102, 12253–12263.

Akaogi, M., Ito, E., Navrotsky, A., 1989. Olivine-modified spinel–spinel transitions in the system Mg_2SiO_4–Fe_2SiO_4: calorimetric measurements, thermochemical calculation, and geophysical application. J. Geophys. Res. 94, 15671–15685.

Bai, Q., Kohlstedt, D.L., 1993. Effects of chemical environment on the solubility and incorporation mechanism for hydrogen in olivine. Phys. Chem. Miner. 19, 460–471.

Christensen, U.R., Yuen, D.A., 1984. The influence of a subducting lithospheric slab with a chemical or phase boundary. J. Geophys. Res. 89, 4389–4402.

Chen, J., Inoue, T., Weidner, D.J., Wu, Y., Vaughan, M.T., 1998. Strength and water weakening of mantle minerals, olivine, wadsleyite and ringwoodite. Geophys. Res. Lett. 25, 575–578.

Chen, J., Li, L., Weidner, D.J., Vaughan, M., 2004. Deformation experiments using synchrotron X-rays: in situ stress and strain measurements a high pressure and temperature. Phys. Earth Planet. Int. 143–144, 347–356.

Evans, B., Goetze, C., 1979. The temperature variation of hardness of olivine and its implication for polycrystaline yield stress. J. Geophys. Res. 84, 5505–5524.

Fei, Y., Mao, H.-K., Shu, J., Parthasarathy, G., Bassett, W.A., Ko, J., 1992. Simultaneous high-P, high-T X ray diffraction study of β-$(Mg,Fe)_2SiO_4$ to 26 GPa and 900 K. J. Geophys. Res. 97, 4489–4495.

Gasparik, T., 1990. A thermodynamic model for the enstatite–diopside join. Am. Mineral. 75, 1080–1091.

Gasparik, T., 1996. Melting experiments on the enstatite–diopside join at 70–240 kbar, including the melting of diopside. Contrib. Mineral. Petrol. 124, 139–153.

Gottstein, G., Mecking, H., 1985. Recrystallization. In: Wenk, H.-R. (Ed.), Preferred Orientation in Deformed Metals and Rocks: An Introduction to Modern Texture Analysis. Academic Press, Orlando, pp. 183–218.

Green II, H.W., Borch, R.S., 1987. The pressure dependence of creep. Acta Metall. 35, 1301–1305.

Guyot, F., Wang, Y., Gillet, P., Ricard, Y., 1996. Quasi-harmonic computations of thermodynamic parameters of olivines at high-pressure and high-temperature. A comparison with experiment data. Phys. Earth Planet. Int. 98, 17–29.

Huang, X., Xu, Y., Karato, S., 2005. Water content in the transition zone from electrical conductivity of wadsleyite and ringwoodite. Nature 434, 746–749.

Inoue, T., Tanimoto, Y., Irifune, T., Suzuki, T., Fukui, H., Ohtaka, O., 2004. Thermal expansion of wadsleyite, ringwoodite, hydrous wadsleyite and hydrous ringwoodite. Phys. Earth Planet. Int. 143–144, 279–290.

Irifune, T., Ringwood, A.E., 1987. Phase transformations in primitive MORB and pyrolite compositions to 25 GPa and some geophysical implications. In: Manghnani, M.H., Syono, Y. (Eds.), High-Pressure Research in Mineral Physics. American Geophysical Union, Washington, DC, pp. 231–242.

Isaak, D.G., 1992. High-temperature elasticity of iron-bearing olivines. J. Geophys. Res. 97, 1871–1885.

Jackson, I., Rigden, S.M., 1996. Analysis of P–V–T data: constraints on the thermoelastic properties of high-pressure minerals. Phys. Earth Planet. Int. 96, 85–112.

Jacobsen, S.D., Demouchy, S., Frost, D.J., Ballaran, T.B., Kung, J., 2005. A systematic study of OH in hydrous wadsleyite from polarized FT-IR spectroscopy and single-crystal X-ray diffraction: oxygen sites for hydrogen storage in Earth's interior. Am. Mineral. 90, 61–70.

Karato, S., 1987. Scanning electron microprobe observation of dislocation in olivine. Phys. Chem. Miner. 14, 245–248.

Karato, S., 1989. Plasticity-crystal structure systematics in dense oxides and its implications for the creep strength of the Earth's deep interior: a preliminary result. Phys. Earth Planet. Int. 55, 234–240.

Karato, S., Rubie, D.C., 1997. Toward an experimental study of deep mantle rheology: A new multianvil sample assembly for deformation studies under high pressures and temperatures. J. Geophys. Res. 102, 20111–20122.

Karato, S., Lee, K.-H., 1999. Stress–strain distribution in deformed olivine aggregates: inference from microstructural observations and implications for textural development. In: Proceedings of the 12th International Conference on Textures of Materials, pp. 1546–1555.

Karato, S., Jung, H., 2003. Effects of pressure on high-temperature dislocation creep in olivine. Philos. Mag. 83, 401–414.

Karato, S., Paterson, M.S., Fitz Gerald, J.D., 1986. Rheology of synthetic olivine aggregates: influence of grain size and water. J. Geophys. Res. 91, 8151–8176.

Kohlstedt, D.L., Keppler, H., Rubie, D.C., 1996. Solubility of water in the α, β and γ phases of $(Mg, Fe)_2SiO_4$. Contribut. Mineral. Petrol. 123, 345–357.

Kubo, T., Ohtani, E., Kato, T., Shinmei, T., Fujino, K., 1998. Effect of water on the α–β transformation kinetics in San Carlos olivine. Science 281, 85–87.

Li, B., Liebermann, R.C., 2000. Sound velocities of wadsleyite β-$(Mg_{0.88}Fe_{0.12})_2SiO_4$ to 10 GPa. Am. Mineral. 85, 292–295.

Li, B., Liebermann, R.C., Weidner, D.J., 2001. P–V–Vp–Vs–T measurements on wsdsleyite to 7 GPa and 873 K: implications for the 410-km seismic discontinuity. J. Geophys. Res. 106, 30575–30591.

Li, L., Weidner, D.J., Raterron, P., Chen, J., Vaughan, M., 2004a. Stress measurements of deforming olivine at high pressure. Phys. Earth Planet. Int. 143–144, 357–367.

Li, L., Weidner, D.J., Chen, J., Vaughan, M.T., Davis, M., Durham, W.B., 2004b. X-ray strain analysis at high pressure: effect of plastic deformation in MgO. J. Appl. Phys. 95, 8357–8365.

Li, L., Weidner, D., Raterron, P., Chen, J., Vaughan, M., Mei, S., Durham, W., 2006a. Deformation of olivine at mantle pressure using the D-DIA. Eur. J. Mineral. 18, 7–9.

Li, Li., Long, H., Raterron, P., Weidner, D., 2006b. Plastic flow of pyrope at mantle pressure and temperature. Am. Mineral. 91, 517–525.

Mayama, N., Suzuki, I., Saito, T., Ohno, I., Katsura, T., Yoneda, A., 2004. Temperature dependence of elastic moduli of β-$(Mg, Fe)_2SiO_4$. Geophys. Res. Lett. 31, doi:10.1029/2003GL019247.

Mei, S., Kohlstedt, D.L., 2000a. Influence of water on plastic deformation of olivine aggregates. Part 1. Diffusion creep regime. J. Geophys. Res. 105, 21457–21469.

Mei, S., Kohlstedt, D.L., 2000b. Influence of water on plastic deformation of olivine aggregates. Part 2. Dislocation creep regime. J. Geophys. Res. 105, 21471–21481.

Nishihara, Y., Shinmei, T., Karato, S., 2006. Grain-growth kinetics in wadsleyite: Effects of chemical environment. Phys. Earth Planet. Int. 154, 30–43.

Nishihara, Y., Shinmei, T., Karato, S., 2008. Effect of chemical environment on the hydrogen-related defect chemistry in wadsleyite. Am. Mineral., in press.

Odqvist, F.K.G., 1974. Mathematical Theory of Creep and Creep Rupture, 2nd ed. Oxford University Press, U.K, 200 pp.

Paterson, M.S., 1982. The determination of hydroxyl by infrared absorption in quartz, silicate glasses and similar materials. Bull. Minéral. 105, 20–29.

Raterron, P., Wu, Y., Weidner, D.J., Chen, J., 2004. Low-temperature olivine rheology at high pressure. Phys. Earth Planet. Int. 145, 149–159.

Sharp, T.G., Bussod, G.Y.A., Katsura, T., 1994. Microstructures in β-$Mg_{1.8}Fe_{0.2}SiO_4$ experimentally deformed at transition-zone conditions. Phys. Earth Planet. Int. 86, 69–83.

Singh, A.K., Balasingh, C., Mao, H.-K., Hemley, R.J., Shu, J., 1998. Analysis of lattice strains measured under nonhydrostatic pressure. J. Appl. Phys. 83, 7567–7575.

Suzuki, I., 1975. Thermal expansion of periclase and olivine, and their anharmonic properties. J. Phys. Earth 23, 145–159.

Suzuki, I., Ohtani, E., Kumazawa, M., 1980. Thermal expansion of modified spinel, β-Mg_2SiO_4. J. Phys. Earth 28, 273–280.

Thurel, E., Cordier, P., 2003. Plastic deformation of wadsleyite. Part I. High-pressure deformation in compression. Phys. Chem. Miner. 30, 256–266.

Thurel, E., Cordier, P., Frost, D., Karato, S., 2003. Plastic deformation of wadsleyite. Part II. High-pressure deformation in shear. Phys. Chem. Miner. 30, 267–270.

Van Houtte, P., Wagner, F., 1985. Development of texture by slip and twinning. In: Wenk, H.-R. (Ed.), Preferred Orientation in Deformed Metals and Rocks: An Introduction to Modern Texture Analysis. Academic Press, Orlando, pp. 233–258.

Wang, Y., Durham, W.B., Getting, I., Weidner, D.J., 2003. The deformation-DIA: a new apparatus for high temperature triaxial deformation to pressures up to 15 GPa. Rev. Sci. Inst. 74, 3002–3011.

Wegner, M.W., Christie, J.M., 1985. General chemical etchants for microstructures and defects in silicates. Phys. Chem. Miner. 12, 90–92.

Weidner, D.J., Li, L., Davis, M., Chen, J., 2004. Effect of plasticity on elastic modulus measurements. Geophys. Res. Lett. 31, doi:10.1029/2003GL019090.

Xu, Y., Nishihara, Y., Karato, S., 2005. Development of a rotational Drickamer apparatus for large-strain deformation experiments under deep Earth conditions. In: Chen, J., Wang, Y., Duffy, T., Shen, G., Dobrzhinetskaya, L.F. (Eds.), Advances in High-Pressure Techniques for Geophysical Applications. Elsevier Science, Amsterdam, pp. 167–182.

Yamazaki, D., Karato, S., 2001. High-pressure rotational deformation apparatus to 15 GPa. Rev. Sci. Inst. 72, 4207–4211.

Zha, C.-s., Duffy, T.S., Mao, H.-k., Downs, R.T., Hemley, R.J., Weidner, D.J., 1997. Single-crystal elasticity of β-Mg_2SiO_4 to the pressure of the 410 km seismic discontinuity in the Earth's mantle. Earth Planet. Sci. Lett. 147, E9–E15.

Zhang, S., Karato, S., Fitz Gerald, J., Faul, U.H., Zhou, Y., 2000. Simple shear deformation of olivine aggregates. Tectonophysics 316, 133–152.